Chinese Chemical Letters 37 (2026) 112846

Contents lists available at ScienceDirect

Chinese Chemical Letters

journal homepage: www.elsevier.com/locate/cclet

Ultrasound-augmented chemodynamic and chemotherapy amplify cascade oxidative stress for potentiating immunogenic cell death in pancreatic cancer treatment

Meng Pan[a], Dong Mo[b], Wen Chen[a], Yun Yang[c], Qingya Liu[d], Yujia Wei[a], Xicheng Li[a], Hanzhi Deng[a], Yan Yu[e], Liping Yuan[a,f], Yu Liu[a], Zhiyong Qian[a,*]

[a] Department of Biotherapy, Cancer Center and State Key Laboratory of Biotherapy, West China Hospital, Sichuan University, Chengdu 610041, China
[b] Department of Radiology, Chongqing General Hospital, Chongqing University, Chongqing 401147, China
[c] Research Laboratory of Plastic and Burns Surgery, West China Hospital, Sichuan University, Chengdu 610041, China
[d] Department of General Surgery, Xinqiao Hospital, Army Medical University, Chongqing 400037, China
[e] Department of Chemistry, Xihua University, Chengdu 610039, China
[f] Chongqing Institute for Food and Drug Control, Chongqing 401121, China

ARTICLE INFO

Article history:
Received 13 February 2026
Revised 24 April 2026
Accepted 27 April 2026
Available online 27 April 2026

Keywords:
Pancreatic cancer
Reactive oxygen species
Chemotherapy
Chemodynamic therapy
Ultrasound
Immunogenic cell death

ABSTRACT

Pancreatic cancer (PCa) is highly aggressive and resistant to conventional therapies due to its dense stroma and immunosuppressive microenvironment. To overcome these barriers, we engineered dextran-coated copper peroxide-doxorubicin nanoclusters (DCPD NCs) that enabled ultrasound (US)-augmented chemodynamic therapy (CDT) and chemotherapy. In the acidic tumor microenvironment, DCPD NCs disassemble and co-release Cu^{2+}, doxorubicin, and self-supplied H_2O_2. Cu^{2+} depletes glutathione (GSH) and catalyzes H_2O_2 to generate $^{\bullet}OH$ with US (1.5 fold higher than that without US). Under US treatment, DCPD NCs not only increased the permeability of Panc02 tumor spheroids, but also increased intracellular reactive oxygen species by 2.1 times, depleted GSH by up to 25.2 %, and induced lipid peroxidation. This nanoplatform works synergistically to induce potent immunogenic cell death. In both subcutaneous and orthotopic PCa mice models, this nanoplatform demonstrated remarkable therapeutic effects. The tumor weights of mice treated with DCPD NCs + US were significantly reduced by 91.8 % and 85.7 % *vs.* controls, with robust calreticulin (CRT) exposure and HMGB1 translocation in tumors. This work establishes an US augmented and self-reinforcing nanoplatform that overcomes stromal and metabolic barriers in PCa, providing a synergistic strategy for catalytic immunotherapy.

© 2026 Published by Elsevier B.V. on behalf of Chinese Chemical Society and Institute of Materia Medica, Chinese Academy of Medical Sciences.

Pancreatic cancer (PCa) is represents one of the most malignant and fatal types of solid malignancies, characterized by a poor 5-year overall survival rate as low as 13 % [1]. Conventional therapies, such as chemotherapy, surgical resection, and immunotherapy, demonstrate limited efficacy for PCa treatment, primarily attributable to its intrinsic immune resistance and suppressive tumor microenvironment (TME) [2]. The key characteristics of TME in PCa include dense stromal components, inadequate vascularization, and profound immune suppression [3–5]. Notably, the abnormal buildup of extracellular matrix (ECM) components creates substantial physical obstacles that significantly impair the penetration and distribution of therapeutic compounds within tumor tissues, consequently diminishing the effectiveness of conventional treatments. Furthermore, the TME of PCa exhibits strong immunosuppressive properties, where tumor cells recruit and activate cells capable of suppressing antitumor immunity and promoting therapeutic resistance [6–8]. Recent advancements in cancer treatment have introduced innovative approaches including photothermal and photodynamic therapies, which demonstrate promising clinical applications, yet their therapeutic efficacy face significant constraints due to light's limited penetration depth in biological tissues and insufficient accumulation of therapeutic compounds within deeply located pancreatic malignancies [9–12]. In summary, there is an imperative need to develop novel synergistic therapies integrating multiple mechanisms to achieve deep-tissue targeting, reverse immunosuppression, and ultimately improve therapeutic outcomes in PCa.

Chemodynamic therapy (CDT), is an emerging antitumor strategy that harnesses Fenton or Fenton-like reactions to transform intracellular endogenous hydrogen peroxide (H_2O_2) into highly cyto-

* Corresponding author.
E-mail address: zhiyongqian@scu.edu.cn (Z. Qian).

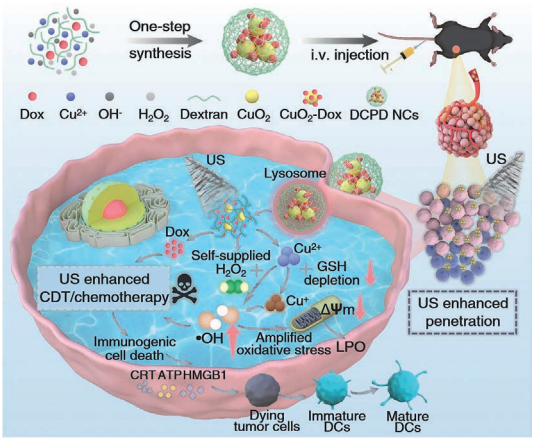
https://doi.org/10.1016/j.cclet.2026.112846
1001-8417/© 2026 Published by Elsevier B.V. on behalf of Chinese Chemical Society and Institute of Materia Medica, Chinese Academy of Medical Sciences.

toxic hydroxyl radicals (•OH) [13–17]. Leveraging the intrinsic overexpression of H_2O_2 in the TME, •OH is generated with enhanced efficiency, a process that not only augments the selective cytotoxicity against tumor cells but also mitigates the potential off-target toxicity to normal cells. Additionally, unlike phototherapy, CDT does not require external energy, enabling superior penetration and therapeutic efficacy in deep-seated tumors or those with inadequate vascular supply. Nevertheless, CDT still faces several critical challenges. First, although tumor regions exhibit higher H_2O_2 levels than healthy tissues, the endogenous H_2O_2 concentration within tumors may still be insufficient to produce adequate •OH. Second, it is difficult to effectively delivery metal ions to tumor sites and sustain their effective concentrations for Fenton or Fenton-like reactions. Finally, a substantial amount of endogenous glutathione (GSH) in tumors rapidly scavenge •OH, significantly compromising the therapeutic potential of CDT.

To overcome the insufficient H_2O_2 supply, several strategies for enhancing CDT based on endogenous or exogenous stimuli have been proposed. Notably, copper peroxide (CuO_2), a Fenton-like metal peroxide nanomaterial, is capable of generating Cu^{2+} and H_2O_2 in the acidic tumor condition, thereby enabling CDT with self-sustained H_2O_2 supply and depletion of GSH to improve reactive oxygen species (ROS) [18–20]. CuO_2 also exerts a synergistic enhancement effect when combined with other therapeutic methods. For instance, Zhu *et al.* [21] engineered multifunctional CuO_2 nanoparticles that integrated self-sustaining CDT with photothermal therapy. Furthermore, studies have demonstrated that the clinically employed anticancer agent doxorubicin (Dox) can synergize with copper-based CDT, leading to superior anticancer outcomes [21–25]. This synergistic effect arises from the dual roles of Dox: It not only directly kills tumor cells but also triggers immunogenic cell death (ICD), thereby stimulating antitumor immune responses.

Nevertheless, the significant biological hazards posed by metal peroxide nanoparticles restrict their broader use in biomedical applications. Therefore, overcoming biological toxicity is crucial for further utilizing metal peroxide nanoparticles to enhance CDT. The strategy of exogenous triggering enhancement of CDT was to use exogenous energy to promote the efficacy of CDT or directly generate ROS to enhance CDT. For example, near-infrared (NIR) light and X-rays were used to enhance CDT [26–28]. Even if these strategies successfully enhance CDT, the low penetration depth of light and the radiation risk associated with X-rays limit their development. Fortunately, the ultrasound (US), which has both the low bio-toxicity of NIR light and the high penetration depth of X-rays, has emerged as a promising exogenous energy for enhancing CDT [29–32]. Under US irradiation, the pressure and temperature of the local microenvironment within tumors increase, thereby facilitating the enhancement of the Fenton reaction. Thus, there is a critical requirement to design innovative nanozyme exhibiting excellent biocompatibility, which can simultaneously generate H_2O_2 and deplete GSH, making them suitable for US-enhanced CDT applications.

Inspired by this, polysaccharide dextran-coated copper peroxide-Dox nanoclusters (DCPD NCs) were designed for enhanced PCa treatment through US-augmented chemotherapy and CDT in this study (Scheme 1). DCPD NCs were fabricated through one-step synthetic approach using dextran, Dox, and Cu^{2+} in the presence of H_2O_2. Upon exposure to the acidic and reductive TME, DCPD NCs undergo decomposition to release Dox, H_2O_2, and Cu^{2+}. These released components exhibit individual antitumor activities and act synergistically to achieve highly efficient antitumor efficacy. Specifically, the released Cu^{2+} depletes intracellular GSH and is reduced to Cu^{+}, which then reacts with both endogenous and self-supplied H_2O_2 to generate •OH. This process amplifies oxidative stress and induces ICD in tumor cells. Following intravenous injection, the DCPD NCs accumulate in both subcutaneous and orthotopic Panc02 tumors *via* the enhanced permeability and retention (EPR) effect. A sequential US activation strategy was further incorporated to address the poor tumor penetration of nanotherapeutics and realize on-demand therapeutic activation, laying the groundwork for maximizing the synergistic efficacy of CDT and chemotherapy. The first US irradiation improves the tumor penetration of DCPD NCs, while the second US irradiation triggers the activation of tumor-localized NCs to generate ROS. When combined with Dox-mediated chemotherapy, this synergistically elicits ICD. This multimodal therapeutic strategy is anticipated to effectively overcome the major limitations of conventional CDT and chemotherapy. Collectively, this US-enhanced, and self-amplifying nanoplatform lays a foundation for a translatable therapeutic approach capable of disrupting both stromal and immunosuppressive barriers in PCa. Moreover, it serves as a promising strategy for combination with immunotherapy to elicit durable antitumor responses.



Scheme 1. Schematic illustration of the preparation of the US-enhanced ROS nanoamplifier, DCPD NCs, and its synergistic chemo/chemodynamic therapy against pancreatic cancer.

Firstly, a series of acid-responsive nanoclusters with different amounts of Dox was prepared successively *via* a one-step reaction according to the previous report [33]. Initial experiments revealed that when the Dox feeding quantity was elevated from 0 mg to 10 mg, the hydrodynamic diameter of the resulting DCPD NCs, as measured through dynamic light scattering (DLS) analysis, expanded from (101.0 ± 1.7) nm to (2567.0 ± 103.1) nm. Notably, other parameters including polydispersity index (PDI), encapsulation efficacy (EE) of Dox, and Cu contents determined by ICP-OES showed no significant change (Table S1 in Supporting information).

Based on this, DCPD5 was selected for subsequent characterization and application. The transmission electron microscope (TEM) images of dextran-coated copper peroxide (DCP) NCs in Fig. 1A and Fig. S1A (Supporting information) demonstrated that copper peroxide nanodots were embedded within dextran matrices, forming clustered structures, and DCPD NCs showed a similar morphology with a larger size according to the TEM images in Fig. 1B and Fig. S1B (Supporting information). Moreover, atomic force microscopy (AFM) imaging was utilized to characterize DCP NCs, which exhibited similar morphology to the TEM characterization (Figs. S1C and D in Supporting information).

Additionally, the crystalline properties and phase composition of DCP and DCPD NCs were examined through powder X-ray diffraction (XRD) techniques. As shown in Fig. 1C, the presence of a single broad diffraction peak indicated the amorphous nature of both DCP and DCPD NCs. Furthermore, the full-range X-ray photoelectron spectroscopy (XPS) spectrum (Fig. 1D) identified the elemental composition, showing Cu, C, and O in both DCP and DCPD

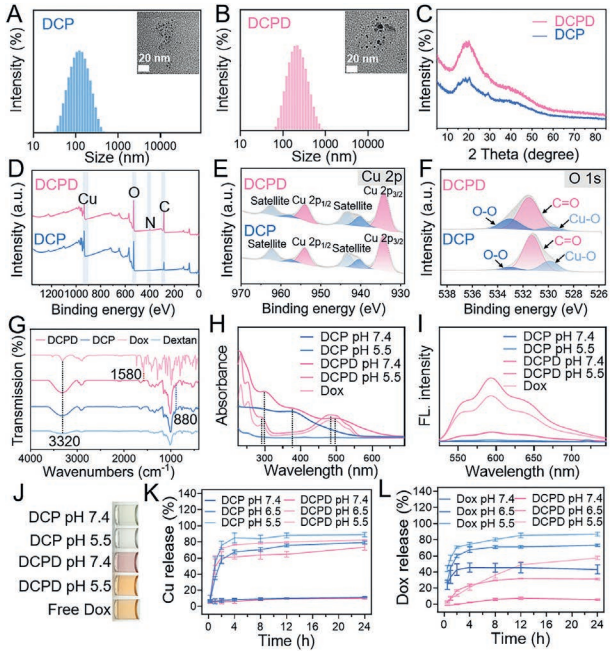


Fig. 1. Characterizations of the nanoclusters. DLS measuring particle size and TEM images of (A) DCP and (B) DCPD NCs. Scale bar: 20 nm. (C) XRD patterns of DCP and DCPD NCs. (D) Survey XPS spectrum of DCP and DCPD NCs. High-resolution Cu 2p (E) and O 1s (F) XPS spectra of DCP and DCPD NCs. (G) FT-IR spectra of dextran, DCP, DCPD, and Dox. (H) UV–vis spectra of Dox, DCP, and DCPD NCs (in different pH). (I) Fluorescence spectra of free Dox, DCP, and DCPD NCs (in different pH). (J) Photographs of free Dox, DCP, and DCPD NCs in different pH solutions. (K) Release of Cu^{2+} from DCP and DCPD NCs at pH 7.4, 6.5, and 5.5. (L) The accumulated release of Dox from free Dox and DCPD NCs at pH 7.4, 6.5, and 5.5. Data are presented as mean ± standard deviation (SD) ($n = 3$).

NCs, whereas the N element was exclusively detected in DCPD NCs, confirming the successful incorporation of Dox (which contains N-containing functional groups). High-resolution XPS spectrum of Cu 2p (Fig. 1E) displayed two characteristic peaks at binding energies of 934 and 954 eV, along with distinct shakeup satellite peaks corresponding to Cu^{2+}. This confirms that Cu^{2+} existed in both DCP and DCPD NCs. Meanwhile, the high-resolution O 1s XPS spectrum (Fig. 1F) was deconvoluted into three distinct peaks, which were respectively assigned to O–O, C=O, and Cu-O. These findings provide evidence for the successful incorporation of dextran and the retention of peroxyl groups in the fabricated nanomaterials. Fourier transform infrared (FT-IR) spectroscopy (Fig. 1G) was conducted to elucidate the interaction mechanism among dextran, Dox, and copper peroxide in DCPD NCs. Both spectral analysis of DCP and DCPD NCs displayed characteristic peaks at 3320 cm^{-1} (O–H stretching) and 1400–1100 cm^{-1} (C–O stretching and C–O–C asymmetric stretching), which were consistent with the characteristic infrared fingerprint of dextran. Moreover, a characteristic peak at 880 cm^{-1} was observed in the FT-IR spectra of both DCP and DCPD NCs, corresponding to the -O–O- stretching vibration of copper peroxide (blue line). Furthermore, the DCPD spectrum displayed a distinctive absorption at 1580 cm^{-1} (marked in red), corresponding to Dox's molecular signature. These spectroscopic observations provide conclusive evidence for the effective integration of Dox molecules into the DCP matrix during the formation of DCPD nanocomposites.

Furthermore, the successful encapsulation of Dox within DCPD NCs and their pH-dependent degradation characteristics were confirmed through ultraviolet-visible (UV–vis) and fluorescence spectroscopic analyses. As shown in Fig. 1H, DCP NCs in pH 7.4 showed an obvious shoulder peak at 375 nm, whereas this spectral signature disappeared under acidic condition (pH 5.5), indicating the decomposition of copper peroxide. For DCPD NCs in pH 7.4, the spectrum showed a shoulder peak at 375 nm, similar to the curve of DCP NCs, demonstrating the existence of CuO_2 in DCPD NCs. Furthermore, UV–vis spectroscopy analysis revealed that both Dox and DCPD NCs exhibited distinct absorption bands at ~300 nm and in the 450–700 nm range. Specifically, Dox displayed two maximum absorption peaks at 288 and 480 nm, whereas DCPD NCs suspended in pH 7.4 buffer exhibited dual absorption maxima at 297 and 495 nm. The spectroscopic analysis confirmed the effective encapsulation of Dox within the nanodot structures. The observed red shift in DCPD NCs demonstrated that intermolecular interactions between Dox and CuO_2 induced the generation of extended conjugated architectures. Importantly, the coordination between Dox and Cu^{2+} significantly quenched its fluorescence, while acidic conditions triggered the breakdown of this coordination complex, restoring the fluorescent properties (Fig. 1I). Moreover, DCPD NCs in pH 5.5 exhibited the same color and absorbance characteristics as Dox, demonstrating the release of Dox (Fig. 1J).

To systematically assess the acid-responsive release behavior, DCP or DCPD NCs were separately dispersed in phosphate buffered solution (PBS) at different pH. Figs. 1K and L demonstrate distinct release patterns for both Cu^{2+} and Dox, showing minimal and gradual release at neutral conditions (pH 7.4). However, when exposed to acidic condition (pH 5.5), a significantly faster and more substantial release occurred. Specifically, DCPD NCs displayed favorable stability at pH 7.4, releasing merely 10 % of Cu^{2+} and 6 % of Dox over a 24 h incubation period. While under acidic conditions, DCPD NCs exhibited a markedly accelerated release kinetics, with the cumulative release of Cu^{2+} and Dox reaching nearly 80 % and 60 %, respectively, within 24 h incubation. This pH-responsive release profile of DCPD NCs is anticipated to potentiate the therapeutic efficacy against tumor tissues while mitigating off-target cytotoxicity toward normal cells. Moreover, the DCPD NCs at pH 7.4 maintained stable hydrodynamic size and PDI over 24 h, indicating good physiological stability. At pH 5.5, their size dropped sharply within 4 h and PDI rose markedly, suggesting rapid disassembly (Fig. S2A in Supporting information). TEM image confirmed acidic-triggered dissociation and morphological breakdown (Fig. S2B in Supporting information). The DLS particle size changes and TEM results of the DCPD NCs were consistent with the acid-responsive drug release behavior of the nanoclusters.

After DCP degradation in an acidic environment, the acid-triggered Cu^{2+}-driven CDT process and US-enhanced $^{\bullet}OH$ generation *in vitro* were shown in Fig. 2A. Firstly, the H_2O_2 self-supplying ability of DCP and DCPD NCs was validated by the $KMnO_4$-based colorimetric method. As presented in Fig. 2B, upon the addition of DCP or DCPD NCs, the UV–vis absorption and characteristic purple color of the $KMnO_4$ gradually diminished and eventually vanished. This is attributed to a H_2O_2-mediated redox process, wherein the purple potassium MnO_4^- was reduced to colorless Mn^{2+}. To further elucidate the correlation between pH conditions and H_2O_2 release capacity, a colorimetric assay based on horseradish peroxidase (HRP) and 2,2′-azino-bis(3-ethylbenzothiazoline-6-sulfonic acid) (ABTS) was utilized to detect H_2O_2. The H_2O_2 can be decomposed into free radicals catalyzed by HRP, and free radicals can be captured by ABTS to produce green-colored $ABTS^{+\bullet}$. The absorbance spectra and digital photographs showed that no H_2O_2 was detected in the solution at pH 7.4 (Fig. S3A in Supporting information), while a substantial amount of H_2O_2 was produced at pH 6.5 (Fig. S3B in Supporting information) and pH 5.5 (Fig. 2C). Moreover, US treatment could further accelerate the generation of H_2O_2 under acidic conditions (Fig. 2D).

Secondly, Cu^{2+} derived from the degradation of DCPD NCs is capable of reacting with GSH to yield Cu^{+}, which can subsequently react with H_2O_2 to generate a substantial quantity of $^{\bullet}OH$. US stimulation can enhance the Fenton reaction, further amplifying $^{\bullet}OH$ generation. To investigate this process, 5,5′-dithiobis-

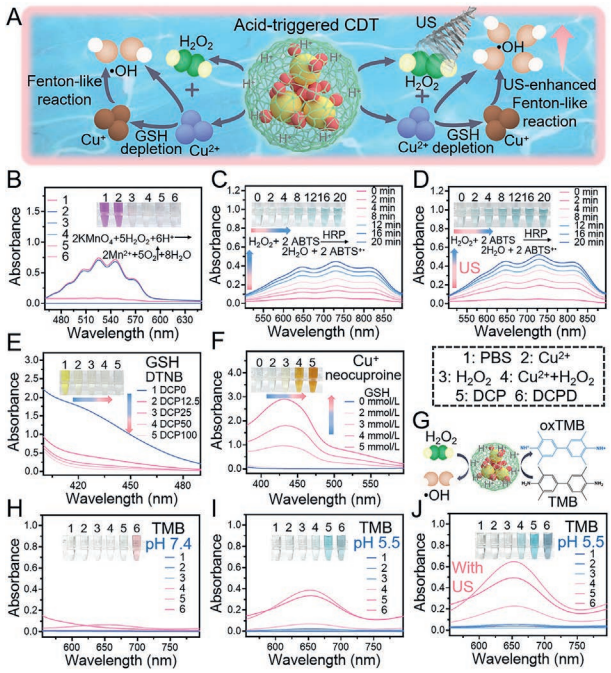


Fig. 2. Acid-triggered and US-enhanced CDT in solution. (A) Schematic diagram of acid-triggered CDT and US-enhanced Fenton-like reaction. (B) Absorption spectra and digital photo of acidic $KMnO_4$ solution after mixing with different sample solutions. Time-dependent absorption spectra and digital photos of ABTS and HRP mixed with DCP NCs at pH 5.5 (C) without or (D) with US irradiation. (E) DCP NCs concentration-dependent absorption spectra of DTNB. (F) GSH concentration-dependent absorption spectra and digital photo of neocuproine with DCP NCs. (G) Schematic illustration of the TMB assay for detecting •OH. Absorption spectra and digital photos of TMB after mixing with different sample solutions at pH 7.4 (H), pH 5.5 (I), and pH 5.5 with US irradiation (J).

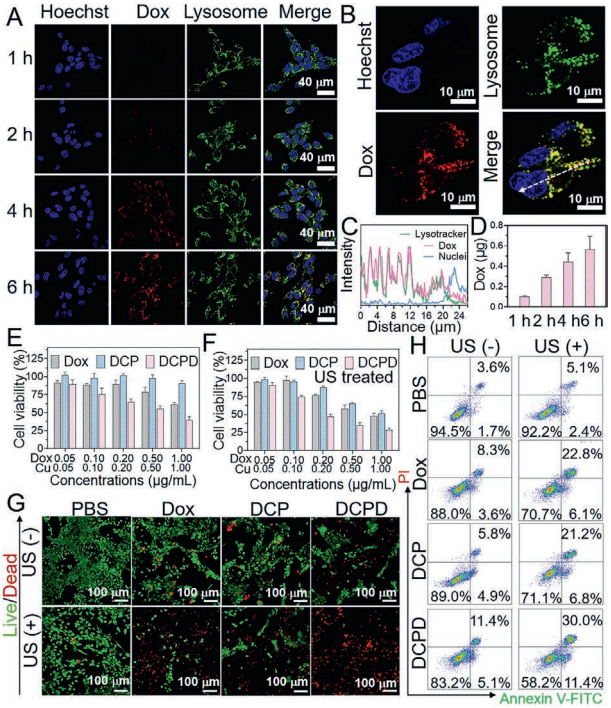


Fig. 3. Cellular uptake and cytotoxicity. (A) CLSM images showing lysosomal colocalization of DCPD NCs in Panc02 cells after 1, 2, 4, and 6 h of incubation. Scale bar: 40 μm. (B) Lysosome colocalization of DCPD NCs-treated Panc02 cells for 6 h. Scale bar: 10 μm. (C) Lysosome colocalization curve of Panc02 cells treated with DCPD NCs for 6 h. (D) The quality of Dox in Panc02 cells treated with DCPD NCs for 1, 2, 4, and 6 h. Data are expressed as mean ± SD ($n = 3$). Cell viability assessment of Panc02 cells exposed to varying doses of Dox, DCP, and DCPD NCs without US (E) or with US (F). Data are expressed as mean ± SD ($n = 6$). (G) Fluorescence images of live (green) and dead (red) Panc02 cell populations. Scale bar: 100 μm. (H) Apoptotic response evaluation in Panc02 cells treated with PBS, Dox, DCP, and DCPD NCs with or without US treatment.

2-(nitrobenzoic acid) (DTNB) was utilized as a probe to measure the GSH consumption capability of both DCP and DCPD NCs, as determined by UV–vis spectra (Fig. 2E and Fig. S4 in Supporting information), indicating the efficient depletion of GSH. To further demonstrate the GSH-mediated valence state transformation from Cu^{2+} to Cu^+, the neocuproine was utilized as the probe because it could form yellow complexes with Cu^+. As shown in Fig. 2F and Fig. S5 (Supporting information), GSH concentration-dependent Cu^+ generation was observed after mixing the acidic DCP or DCPD solution with different concentrations of GSH.

Lastly, the •OH generating capacity of DCP and DCPD NCs was investigated by 3,3′,5,5′-tetramethylbenzidine (TMB) chromogenic test. This method relies on the fact that TMB undergoes oxidation when exposed to highly reactive •OH, producing a distinct blue-green coloration. The oxidized form of TMB (oxTMB) displays maximum absorption around 650 nm (Fig. 2G). Experimental results presented in Figs. 2H and I and Fig. S6 (in Supporting information), neither Cu^{2+} nor H_2O_2 alone exerted any detectable effect on the absorbance enhancement of TMB, irrespective of neutral or acidic conditions. In contrast, the combination of Cu^{2+} and H_2O_2 triggered a pronounced and rapid chromogenic shift of the aqueous TMB solution under acidic conditions (pH 5.5). This observation confirms the excellent Fenton-like catalytic performance of Cu^{2+} and their ability to effectively produce •OH through Cu^{2+}-catalyzed Fenton chemistry. Consistent with predictions, both DCP and DCPD induced visible color alterations in TMB solutions under mild acidic conditions (pH 6.5 and 5.5), but not under neutral conditions (pH 7.4), which could be arisen from the accompanying Fenton-like reaction between their acid-directed dissociation products (Cu^{2+} and H_2O_2). More importantly, the presence of US significantly enhanced the oxidation of TMB which elevated by 1.5-fold compared to DCPD without US irradiation, as shown in Fig. 2J, validating the US enhancement of the Fenton-like reaction.

Prior to evaluating the anticancer activity *in vitro*, the cellular uptake of DCPD NCs was evaluated initially. Extended incubation time between DCPD NCs and Panc02 cells resulted in progressive enhancement of Dox fluorescence intensity and intracellular accumulation (Fig. S7 in Supporting information). As previously discussed, nanoparticles are naturally internalized into lysosomes, and pH-sensitive nanoreactors would be decomposed preferentially within the acidic lysosomes and then leak into the cytoplasm. To demonstrate the acid-responsive of DCPD NCs, the colocalization of DCPD NCs (red) with lysosomes (green) in Panc02 cells following incubation at different time intervals was conducted (Fig. 3A). Notably, DCPD NCs exhibited co-localization with lysosomes starting from 1 h, and the red fluorescence of Dox gradually increased within 6 h (Figs. 3B and C), suggesting the dissociation of DCPD NCs and subsequent release of Dox. Weak mitochondrion and endoplasmic reticulum (ER) co-localization with DCPD NCs, as depicted in Fig. S8 (Supporting information), further confirmed the specific lysosome distribution. Furthermore, a quantitative analysis was conducted to detect the cellular uptake of Dox, and the results were consistent with the fluorescence imaging, showing that the uptake of Dox increased in a time-dependent manner within 6 h incubation (Fig. 3D).

Next, the cytotoxicity was studied by an MTT assay. As dextran was the main component of DCPD NCs, its biosafety was evaluated first. As shown in Fig. S9A (Supporting information), there was negligible cytotoxicity, even when dextran concentrations reached 25 mg/mL. Then, the cytotoxicity of the preparations was studied

at a series of concentrations (Fig. 3E). The DCP NCs exerted low toxicity on the tumor cells at 0.5 μg/mL of copper, whereas DCPD NCs killed nearly half of the cells at the same concentration of copper, due to the introduction of Dox. Moreover, DCPD NCs exhibited higher cytotoxicity than free Dox. Furthermore, following US exposure, all three preparations exhibited diminished cell viability relative to their counterparts without US (Fig. 3F). Moreover, the cytotoxicity of the preparations on 3T3 cells was also evaluated (Fig. S9B in Supporting information). There was negligible cytotoxicity of both DCP and DCPD NCs, even when Cu concentrations reached 4 μg/mL. Consistently, bright-field microscopy images and calcein AM/propidium iodide (PI) dual-staining experiments corroborated that the DCPD NCs combined with US exposure exerted the most prominent therapeutic efficacy relative to all other groups (Fig. 3G and Fig. S10 in Supporting information). These observations were further validated by quantitative assessments of apoptotic rates using flow cytometry (Fig. 3H). Collectively, the cellular experiments demonstrated that DCPD NCs responded to acidic conditions by releasing Dox, thereby achieving a synergistic effect of US-enhanced CDT and *in situ* chemotherapy in cell treatments.

The mechanisms of DCPD NCs in the tumor cells, including US-enhanced cascade oxidative stress and induced immunogenic responses, were further investigated in detail (Fig. 4A). Considering that Fenton catalytic Cu^{2+} can regulate intracellular oxidative stress, the fluorescent probe (DCFH-DA) was employed to quantify ROS production in Panc02 cells across various treatments by confocal laser scanning microscope (CLSM) and flow cytometry. A moderate intracellular ROS fluorescence signal was detected in Dox-treated cells, attributed to the intrinsic redox-modulating properties of Dox (Fig. 4B). Notably, DCP and DCPD NCs elicited markedly enhanced intracellular green fluorescence indicative of elevated ROS levels, which stemmed from the dual functionalities of CuO_2, namely its capacity for on-site H_2O_2 self-supply and Cu-mediated CDT. In addition, after US treatment, all experimental groups exhibited higher fluorescence signals, indicating that US has an enhancing effect on ROS generation. Among all experimental conditions, the combination of DCPD NCs with US stimulation exhibited the most intense green fluorescence signal, indicating that the combined approach of US-augmented CDT and Dox-mediated chemotherapy achieved the highest CDT performance. Flow cytometry quantification of intracellular ROS concentrations revealed a parallel pattern (Fig. 4C), which fully corroborated the superior ROS-generating capacity of DCPD NCs under US irradiation, showing a 2.1 times greater ROS production compared to DCPD NCs treatment alone without US activation.

Elevated GSH levels in the TME not only function as an endogenous antioxidant to scavenge excessive ROS but also act as a chelator of Cu^{2+}. Accordingly, the intracellular GSH depletion capacity of DCPD NCs was evaluated, with the corresponding results presented in Fig. 4D. Compared to the control group, cells treated with Dox alone showed minimal alteration in intracellular GSH content. DCPD NCs exhibited a pronounced capacity to deplete intracellular GSH, which could be ascribed to the fact that US facilitated the intracellular release of Cu^{2+}. Flow cytometry measurements of GSH inside cells provided corroborating evidence (Fig. S11 in Supporting information). The combination of DCPD NCs and US irradiation achieved a remarkable intracellular GSH depletion efficiency of 25.2 %. Taken together, these findings conclusively verify that DCPD NCs are capable of perturbing the intracellular redox homeostasis of cancer cells *via* a dual-mode mechanism characterized by US-amplified ROS generation and GSH depletion.

Mitochondria play pivotal roles in the modulation of cellular apoptosis and ROS generation, whereas intracellular ROS accumulation is concomitantly associated with mitochondrial hyper polarization. Given the remarkable capacity of DCPD NCs to induce ROS generation, changes of mitochondrial membrane potential ($\Delta\Psi_m$) within cancer cells were further examined utilizing the JC-1 probe. This sensitive indicator forms red-emitting aggregates when mitochondrial potential remains high, but shifts to green-emitting monomers when depolarization occurs. As presented in Fig. S12 (Supporting information) and Fig. 4E, Panc02 cells exposed to DCPD NCs with US irradiation displayed the most intense green fluorescence signal accompanied by a negligible red fluorescence signal, a hallmark indicative of severe mitochondrial impairment. These observations correlated well with previous measurements of cell viability and oxidative stress levels.

Furthermore, ROS react with diverse intracellular macromolecules, to induce lipid peroxidation (LPO). This process perturbs cell membrane fluidity and permeability, and more critically, impairs the structural integrity of mitochondrial membranes. The lipophilic C11-BODIPY$^{581/591}$ fluorescent probe readily penetrates the lipid bilayer and exhibits a characteristic fluorescence shift from red to green emission when encountering LPO byproducts. The CLSM observations revealed that Panc02 cells treated with DCPD NCs combined with US irradiation exhibited the most prominent enhancement in green fluorescence intensity accompanied by

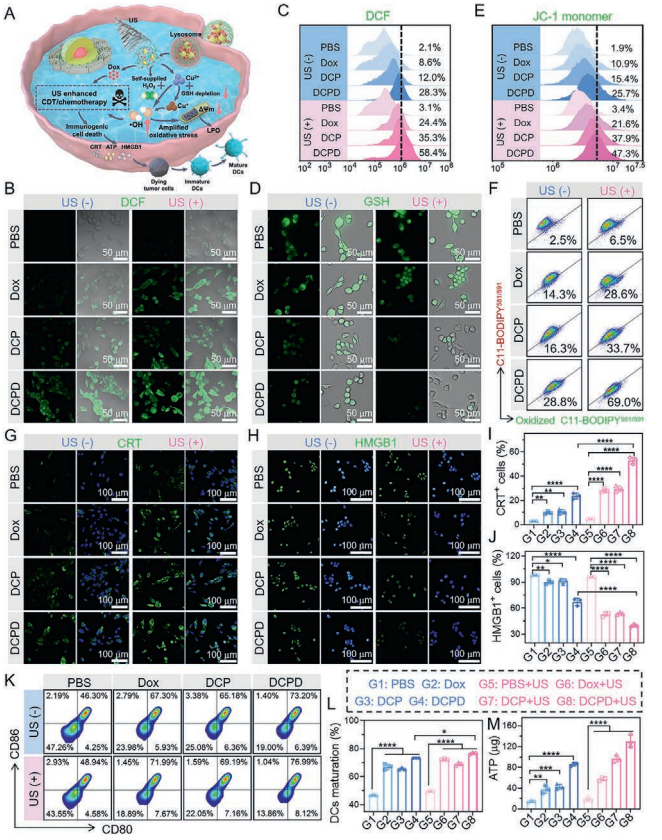


Fig. 4. Potential mechanisms of DCPD-induced oxidative stress and ICD *in vitro*. (A) Schematic illustration of potential mechanisms of DCPD-induced oxidative stress and ICD. (B) CLSM images and (C) flow cytometry of the DCFH-DA probe for detecting intracellular ROS levels in Panc02 cells treated with different samples without or with US irradiation. Scale bar: 50 μm. (D) CLSM images of GSH tracer for detecting intracellular GSH levels in Panc02 cells after incubation with various samples without or with US treatment. Scale bar: 50 μm. (E) Flow cytometry of the JC-1 probe for detecting mitochondrial damage of Panc02 cells after various treatments. (F) Flow cytometry of the C11-BODIPY$^{581/591}$ probe for detecting lipid peroxidation products of Panc02 cells after various treatments. Fluorescent images of CRT (G) and HMGB1 (H) in Panc02 cells incubated with different samples. Scale bar: 100 μm. Flow cytometry of CRT (I) and HMGB1 (J) in Panc02 cells incubated with different samples. (K, L) Flow cytometry analysis of CD80/CD86 expression to detect DC maturation. (M) The extracellular ATP level of Panc02 cells after incubation with different samples. Data are expressed as mean ± SD ($n = 3$). $^{*}P < 0.05$, $^{**}P < 0.01$, $^{***}P < 0.001$, $^{****}P < 0.0001$.

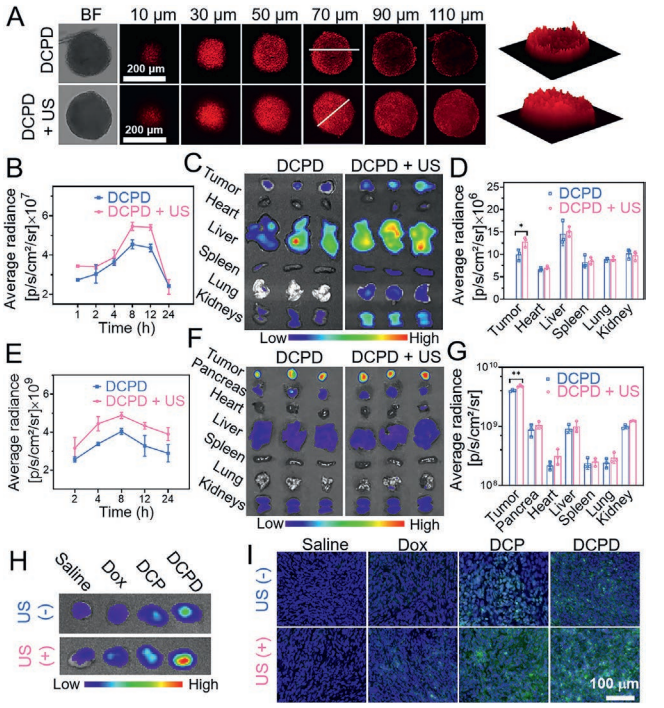


Fig. 5. US-enhanced penetration and biodistribution. (A) Drug penetration in a three-dimensional multicellular tumor sphere analyzed by CLSM, and representative 2.5D profile of fluorescent signals. Scale bar: 200 μm. (B) Semi-quantitative fluorescence intensities of tumors based on *in vivo* fluorescence imaging of subcutaneous tumor-bearing mice. (C) *Ex vivo* fluorescence images after post-injection of nanoparticles over 8 h on the subcutaneous tumor model. (D) Semi-quantitative fluorescence intensities of major organs based on *ex vivo* fluorescence imaging. (E) Semi-quantitative fluorescence intensities of tumors based on *ex vivo* fluorescence imaging of orthotopic tumor-bearing mice. (F) *Ex vivo* fluorescence images and (G) semi-quantitative fluorescence intensities of tumors, pancreas, and major organs of orthotopic tumor-bearing mice after 8 h injection. Data are presented as mean ± SD ($n = 3$). $^{*}P < 0.05$, $^{**}P < 0.01$. (H) *Ex vivo* fluorescence images of tumors stained with the DCFH-DA probe. (I) ROS generation in tumor tissues. Scale bar: 100 μm.

diminished red fluorescence, indicative of robust LPO (Fig. S13 in Supporting information). In addition, flow cytometry analysis further validated the enhanced green fluorescence signal, yielding results consistent with those of fluorescence imaging assays (Fig. 4F).

To confirm if DCPD NCs trigger ICD effects, changes in key damage-associated molecular patterns (DAMPs) were evaluated, including calreticulin (CRT), high-mobility group box 1 (HMGB1), and adenosine triphosphate (ATP). Fluorescence imaging (Figs. 4G and H) and flow cytometry (Figs. 4I and J, Figs. S14 and S15 in Supporting information) consistently showed that Panc02 cells treated with DCPD NCs plus US exhibited the highest CRT surface exposure and nearly complete HMGB1 translocation to the extracellular milieu, compared with other groups. Subsequently, a Transwell model was constructed to establish and to assess the effect of DCPD NCs-induced ICD on dendritic cell (DC) maturation *in vitro*. Using CD80 and CD86 co-stimulation molecules as DC maturation/activation markers, flow cytometry results showed that ~77 % of DCs matured in the DCPD NCs + US group (Figs. 4K and L), a proportion significantly higher than that in other groups. Meanwhile, this combination treatment also resulted in the highest ATP secretion level (Fig. 4M).The above *in vitro* cellular experiments demonstrated that DCPD NCs could induce ICD effects in tumor cells, and US could enhance anti-tumor responses.

To investigate the US-enhanced tumor tissue penetration of DCPD NCs, a 3D Panc02 tumor sphere model was established. Uniform-sized tumor spheres (~200 μm) were employed to assess nanoreactor penetration. As shown in Fig. 5A, following 4 h of incubation, DCPD NCs achieved a penetration depth of ~70 μm in tumor spheres, which increased to ~110 μm post-US irradiation. These results demonstrate that US effectively enhances nanoreactor penetration in tumor spheres.

Next, the *in vivo* distribution of DCPD NCs was investigated. All procedures involving animals were conducted in strict accordance with the ethical standards established by the State Key Laboratory of Biotherapy at West China Hospital, Sichuan University, following approval from the Institutional Animal Care and Use Committee (No. 20250313037). The pharmacokinetics of DCPD NCs were evaluated by quantifying the Dox concentration in circulating blood. Fig. S16 (Supporting information) illustrates that DCPD demonstrated significantly prolonged circulation time and enhanced blood retention compared to unencapsulated Dox, highlighting the nanoparticle's superior ability to avoid rapid clearance from the body. Next, the *in vivo* tumor tropism of DCPD NCs in Panc02 subcutaneous tumor-bearing mice was monitored by an *in vivo* imaging system. As displayed in Figs. 5B and C and Fig. S17 (Supporting information), a distinct fluorescent signal was detected at the tumor site 8 h post-intravenous injection of DCPD NCs, confirming the excellent tumor-targeting ability of the nanoparticles. Moreover, the DCPD NCs plus US showed higher fluorescence intensity (~1.3 folder), demonstrating that US could enhance the accumulation at tumors. The nanoparticles exhibited significant tumor uptake while also showing widespread organ distribution, with the liver and kidneys displaying particularly high accumulation levels. This was confirmed through *ex vivo* imaging analysis and quantitative measurements of fluorescence signals in both tumor tissues and organs (Fig. 5D).

Further investigation into the biodistribution of DCPD NCs was conducted using orthotopic tumor models. As exhibited in Figs. 5E-G, the DCPD NCs + US showed higher fluorescence intensity (~1.2-fold), demonstrating the enhancement of US on drug deep penetration. Moreover, the *ex vivo* tissues were collected for inductively coupled plasma mass spectrometry (ICP-MS) detection. The results in Fig. S18 (Supporting information) were consistent with those of *in vivo* bio imaging. In addition, *in vivo* ROS detection was performed by the DCFH-DA probe. Strong fluorescent signals of tumor tissues and sections were detectable in mice treated with DCPD NCs in conjunction with US irradiation, indicating that CDT and chemotherapy synergistically generate ROS upon US irradiation (Figs. 5H and I).

Building upon the promising *in vitro* tumor inhibition results and US-improved tumor penetration properties of DCPD NCs, further investigations were conducted into their synergistic antitumor performance using Panc02 tumor-bearing mouse models (Fig. 6A). In this *in vivo* therapeutic assessment, male C57BL/6 mice were systematically allocated into 8 groups ($n = 5$): Saline (G1), Dox (G2), DCP (G3), DCPD (G4), saline + US (G5), Dox + US (G6), DCP + US (G7), and DCPD + US (G8). Mice in each group were then administered with the corresponding therapeutic agents. And the US-treated groups (G5-G8) were treated with two US irradiation, including the first US application right after administration to open the tumor barrier, and the second US application 8 h post administration to fully enhance the intratumoral CDT effect. Moreover, the treatment was repeated every two days. Subsequently, tumor growth and excised tumor weights were recorded continuously throughout the experiment.

During the experimental period, the results depicted in Figs. 6B-D demonstrated that tumor progression in the US-only treatment (G5) remained largely unchanged when compared to the saline group (G1). In contrast, all the therapeutic agents plus US treatment groups exhibited higher tumor inhibition, especially the DCPD + US (G8). This finding strongly supported the superior effectiveness of combined chemotherapy and CDT when augmented by US. Notably, tumor weights of mice treated with DCPD under US

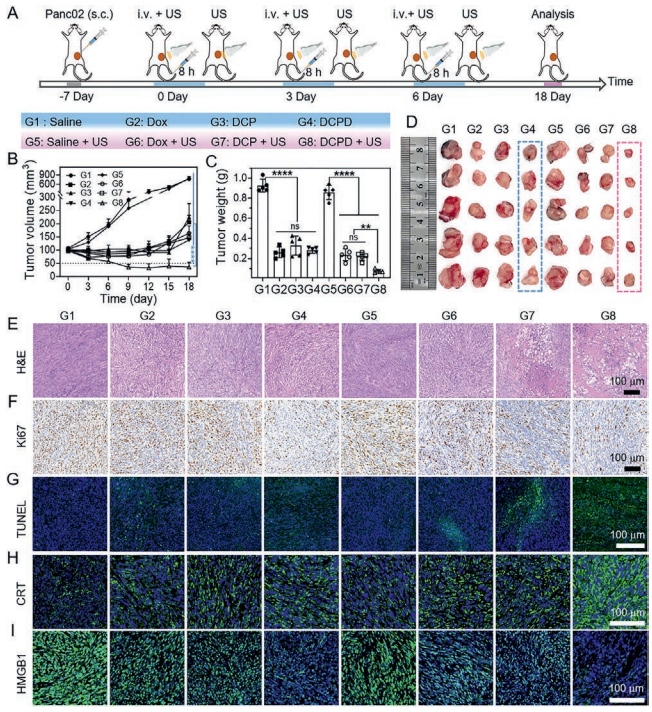


Fig. 6. Evaluation of DCPD-mediated therapy in subcutaneous pancreatic tumor mouse models. (A) Schedule of subcutaneous pancreatic tumor establishment, systemic administrations of therapeutic agents, sequential US treatment, and tumor growth monitoring. (B) Plots of the average tumor volume and (C) tumor weights of mice following the indicated treatments. Data are presented as mean ± SD ($n = 5$). ns, not significant. $^{**}P < 0.01$, $^{****}P < 0.0001$. (D) Photograph of resected tumors on day 18 after indicated treatments. (E) H&E, (F) Ki67, and (G) TUNEL staining of post-treatment mouse tumor sections. (H) CRT and (I) HMGB1 immunofluorescence staining of Panc02 tumor sections at 24 h post-treatment (green fluorescence for CRT and HMGB1). Scale bar: 100 μm.

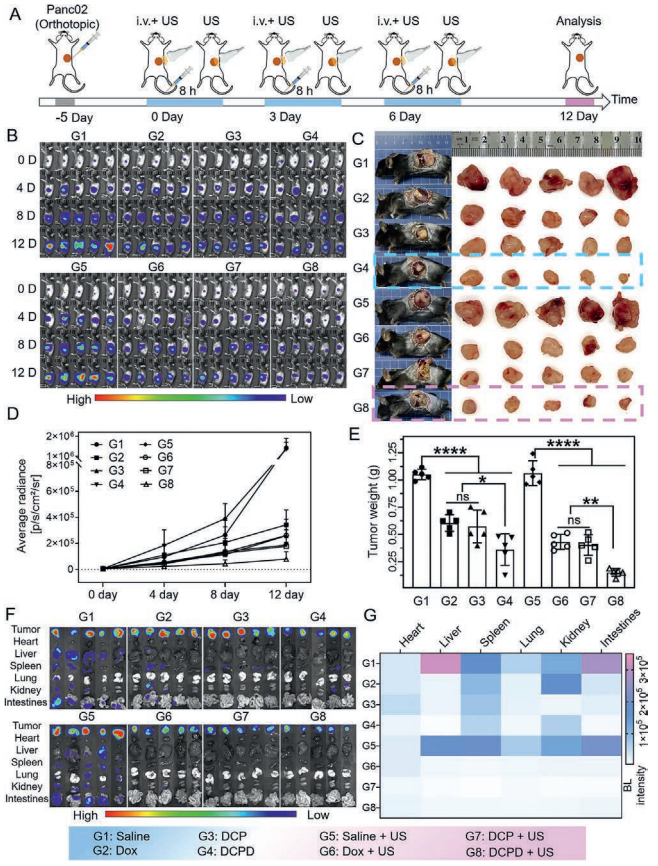


Fig. 7. Evaluation of DCPD-based therapy in orthotopic pancreatic tumor models. (A) Experimental schedule: orthotopic tumor establishment, systemic administration of therapeutic agents, sequential US treatment, and tumor growth monitoring. (B) *In vivo* bioluminescence (BL) images of tumor-bearing mice at various time points. (C) Photographs of mice and resected tumors on day 12 post-treatment. (D) Quantification of tumor BL intensities at different time points. (E) Excised tumor weights post-treatment. (F) *Ex vivo* BL images of tumor and major organs on day 12. (G) Heatmap of BL intensities in tumor and major organs across groups. Data are presented as mean ± SD ($n = 5$). $^{*}P < 0.05$, $^{**}P < 0.01$, $^{****}P < 0.0001$.

irradiation significantly reduced by 91.8 % compared to the Saline. Furthermore, excised tumors were fixed followed by Hematoxylin-Eosin (H&E), terminal deoxynucleotidyl transferase-mediated dUTP nick end labeling (TUNEL), Ki67, CRT, and HMGB1 staining to assess tumor cell necrosis, apoptosis, proliferation, and ICD induction (Figs. 6E-I). Specifically, H&E staining revealed that tumor cells in the DCPD + US (G8) were more sparsely distributed compared with other groups. Additionally, TUNEL and Ki67 staining results showed a higher apoptotic cell ratio and a lower proliferative cell ratio in the DCPD + US (G8) than in the other groups. Furthermore, compared with the saline group, Dox, DCP, and DCPD induced moderate release of HMGB1 and exposure of CRT. Notably, DCPD combined with US irradiation triggered the most pronounced elevation in HMGB1 and CRT levels, demonstrating robust DAMP release into the TME and subsequent activation of anti-tumor immune responses. Moreover, the body weight change of mice injected with DCP and DCPD NCs combined with or without US during the treatments was not significant, while mice in the Dox-treated groups (G2 and G6) experienced substantial body weight loss (Fig. S19 in Supporting information), indicating the relative safety of nanomedicine. Moreover, histological examination of major organs revealed no obvious pathological abnormalities (Fig. S20 in Supporting information), indicating good biocompatibility of this therapy.

Subsequently, the chemo/chemodynamic treatment capabilities of DCPD NCs in deep tissues were assessed by orthotopic Panc02 pancreatic tumor models (Fig. 7A). Tumor progression was monitored *via* tracking bioluminescent (BL) emissions from Panc02-Luc cells. In the absence of US irradiation, monotherapy with Dox or DCP alone afforded minimal tumor growth suppression, whereas US monotherapy even exerted a mild tumor-promoting effect (Figs. 7B and C). Notably, US irradiation significantly enhanced the antitumor efficacy of all therapeutic regimens, with the DCPD + US group demonstrating the most potent efficacy. Tumor BL intensities (Fig. 7D) and excised tumor weights (Fig. 7E) were quantified to confirm therapeutic outcomes; specifically, the DCPD + US group exhibited a significant 85.7 % reduction in tumor weight relative to the saline group. To assess the therapeutic efficacy of this DCPD-based approach in inhibiting tumor growth and preventing metastasis, major organs (including kidneys, lungs, spleen, liver, heart, and intestines) from mice after treatment initiation for 12 days were harvested for BL imaging (Fig. 7F). In both saline groups (with or without US), distinct BL signals consistent with tumor metastasis were detected in all tested organs except the heart and lungs. In contrast, BL signals in these organs were barely detectable in groups receiving therapeutic agents with US. Quantitative analysis further confirmed that US irradiation significantly enhanced the tumor-suppressive effect of the therapeutic regimens (Fig. 7G). Additionally, microscopic analysis of tumor tissue sections through H&E staining provided additional evidence supporting the strong anticancer effects achieved when DCPD were used in conjunction with US (Fig. S21 in Supporting information). H&E staining images of major organs showed that no tumor metastasis was observed in the liver, spleen, and kidneys for the DCPD + US group (Fig. S22 in Supporting information). Moreover, no significant fluctuations in

mouse body weights were noted throughout the treatment period (Fig. S23 in Supporting information), further confirming the good biocompatibility of this strategy.

To further evaluate the biocompatibility of DCPD NCs, the body weight changes of healthy mice treated with different doses were monitored. In the comparison of body weight, slightly substantial variation was observed between all the DCPD NCs groups and the saline group, while no significant changes were monitored among groups with different doses of DCPD NCs (Fig. S24 in Supporting information). Blood specimens were gathered from the mice for hematological and biochemical analyses. Comprehensive safety evaluations revealed that all tested parameters fell within the normal reference range, with no statistically significant differences detected between the DCPD (5 mg/kg) and saline groups (Fig. S25 in Supporting information). Furthermore, H&E staining of major organs (heart, liver, spleen, lungs, and kidneys) demonstrated no noticeable pathological lesions or inflammatory responses in both the DCPD NCs and saline groups (Fig. S26 in Supporting information). Collectively, these findings validated that DCPD NCs exhibited a promising biosafety profile, demonstrating both safety and efficacy for potential clinical applications in future clinical translation endeavors.

To summarize, we have successfully engineered a dextran-decorated nanoplatform, DCPD NCs, for the synergistic treatment of PCa. This system integrates US-enhanced CDT and chemotherapy into a single smart platform. The facile one-step synthesis yields NCs that efficiently achieve preferential tumor localization facilitated by the EPR effect and US enhancement. Upon encountering the acidic and reductive TME, DCPD NCs undergo dissociation to release their therapeutic cargos. These components engage in a powerful self-reinforcing cycle: Cu^{2+} depletes GSH and generates Cu^{+}, which then catalyzes the conversion of both endogenous and self-supplied H_2O_2 into highly toxic $^{\bullet}OH$, amplifying oxidative stress and inducing robust ICD. Concurrently, Dox not only exerts direct cytotoxic effects but also elevates H_2O_2 intracellular levels, thereby fueling the Fenton-like reaction and further enhancing the ICD effect. This multimodal strategy effectively overcomes the limitations of conventional monotherapy, offering a potent approach to disrupt the stromal and immunosuppressive barriers of PCa.

Despite the promising results, several aspects warrant further investigation to advance this nanoplatform towards clinical translation. Future studies will focus on a comprehensive evaluation of the long-term biosafety, biodegradation, and clearance pathways of the DCPD NCs *in vivo*. A deeper mechanistic exploration into how this platform remodels the TME and reverses immunosuppression is also crucial. Furthermore, the potential of DCPD NCs to synergize with existing immunotherapy, such as immune checkpoint inhibitors, represents an exciting frontier. Validating this combination strategy in more advanced preclinical models will be essential to establish its efficacy in eliciting durable antitumor immunity and preventing recurrence. This US-enhanced and self-reinforcing nanoplatform is anticipated to pave a viable and translatable path for combination therapy against PCa.

CRediT authorship contribution statement

Meng Pan: Writing – review & editing, Writing – original draft, Visualization, Validation, Methodology, Investigation, Conceptualization. **Dong Mo:** Writing – review & editing, Validation, Investigation, Data curation, Conceptualization. **Wen Chen:** Visualization, Methodology, Investigation. **Yun Yang:** Supervision, Methodology, Investigation, Data curation. **Qingya Liu:** Supervision, Project administration, Formal analysis, Data curation. **Yujia Wei:** Validation, Investigation. **Xicheng Li:** Visualization, Investigation. **Hanzhi Deng:** Visualization, Investigation. **Yan Yu:** Visualization, Validation, Formal analysis. **Liping Yuan:** Visualization, Investigation. **Yu Liu:** Investigation. **Zhiyong Qian:** Writing – review & editing, Supervision, Resources, Project administration, Funding acquisition.

Declaration of competing interest

The authors declare that they have no known competing financial interests or personal relationships that could have appeared to influence the work reported in this paper.

Acknowledgments

This work was financially supported by the National Natural Science Foundation of China (No. NSFC32530059), the Natural Science Foundation of Sichuan Province (No. 2024NSFSC0046), and 1·3·5 project for disciplines of excellence, West China Hospital, Sichuan University (No. ZYGD24003). We would like to thank Guiping Yuan from the Analytical and Testing Center of Sichuan University for the morphology characterization of nanoparticles by TEM.

Supplementary materials

Supplementary material associated with this article can be found, in the online version, at doi:10.1016/j.cclet.2026.112846.

References

[1] T.F. Stoop, A.A. Javed, A. Oba, et al., Lancet 405 (2025) 1182–1202.
[2] C.J. Halbrook, C.A. Lyssiotis, M. Pasca di Magliano, A. Maitra, Cell 186 (2023) 1729–1754.
[3] P.P. Provenzano, C. Cuevas, A.E. Chang, et al., Cancer Cell 21 (2012) 418–429.
[4] M.A. Jacobetz, D.S. Chan, A. Neesse, et al., Gut 62 (2013) 112–120.
[5] H. Wang, L. Qi, Y.F. Fang, et al., J. Control. Release 388 (2025) 114278.
[6] L.J. Peng, Y.F. Liang, X.N. Guo, et al., Nanoscale Adv. 7 (2025) 5888–5904.
[7] J. Yang, R. Kato, J. Choi, Nanoscale 17 (2025) 22715–22732.
[8] Q.Y. Deng, A. Hua, Q.F. Zhao, et al., Biomaterials 324 (2026) 123501.
[9] P.P. Yang, X. Zhi, Y.X. Xu, et al., Nano Today 51 (2023) 101891.
[10] J.R. Cui, Z.H. Xue, Z.X. Zhang, et al., Adv. Funct. Mater. 36 (2025) e20855.
[11] N.C. Song, G.Q. Tian, H.J. Li, et al., Nano Lett. 25 (2025) 17693–17701.
[12] Z. Hu, J. Meng, MedComm Biomater. Appl. 4 (2025) e70034.
[13] P.R. Zhao, H.Y. Li, W.B. Bu, Angew. Chem. Int. Ed. 65 (2025) e22670.
[14] C. Zhang, W.B. Bu, D.L. Ni, et al., Angew. Chem. Int. Ed. 55 (2016) 2101–2106.
[15] P.H. Wei, X.G. Niu, D.L. Wang, et al., Mater. Today Bio 32 (2025) 101913.
[16] X.L. Cai, Q.H. Zheng, Y. Wu, et al., Chin. Chem. Lett. 37 (2026) 111670.
[17] L.P. Zhao, C.Y. Huang, R.R. Zheng, et al., MedComm Biomater. Appl. 4 (2025) e70024.
[18] L.S. Lin, T. Huang, J. Song, et al., J. Am. Chem. Soc. 141 (2019) 9937–9945.
[19] L. Yu, W.Q. Han, J. Zhang, et al., Chem. Eng. J. 520 (2025) 166043.
[20] W.W. Wu, Y. Yang, Y. Zhang, et al., Chem. Eng. J. 481 (2024) 148113.
[21] H.R. Zhu, C.Q. Huang, J.R. Di, et al., ACS Nano 17 (2023) 12544–12562.
[22] Y.L. Fang, S.S. Huang, Q.Y. Hu, et al., ACS Nano 17 (2023) 24883–24900.
[23] Y. He, X. Tian, M. Zhang, et al., Biomater. Sci. 12 (2024) 5534–5546.
[24] S.X. Hou, Y.E. Gao, X.B. Ma, et al., Chem. Eng. J. 416 (2021) 129037.
[25] Y.X. Xiong, Z.T. Yong, S.Y. Li, et al., Adv. Funct. Mater. 34 (2023) 2310158.
[26] L. Zhao, Y.W. Chen, Q.L. Wei, et al., Chem. Eng. J. 492 (2024) 152265.
[27] A.H. Zhang, W.C. Kong, X.L. Zhang, et al., Nanoscale 17 (2025) 7760–7771.
[28] G.T. Tan, C.Y. Qi, Q.Q. Zhang, et al., J. Control. Release 376 (2024) 899–912.
[29] X.W. Wen, C.X. Wang, S.H. Bi, et al., Small 20 (2024) 2405457.
[30] Q.Q. Sun, Z. Wang, B. Liu, et al., Coord. Chem. Rev. 451 (2022) 214267.
[31] Q.Y. Zhao, Y.C. Zhao, S.J. Zhong, et al., Chin. Chem. Lett. 35 (2024) 109644.
[32] L.P. Yuan, M. Pan, H.Z. Deng, et al., Chin. Chem. Lett. 36 (2025) 110723.
[33] M. Li, X. Lan, X.M. Han, et al., ACS Appl. Mater. Interfaces 13 (2021) 29269–29280.